

Formation of Protein and Protein–Gold Nanoparticle Stabilized Microbubbles by Pressurized Gyration

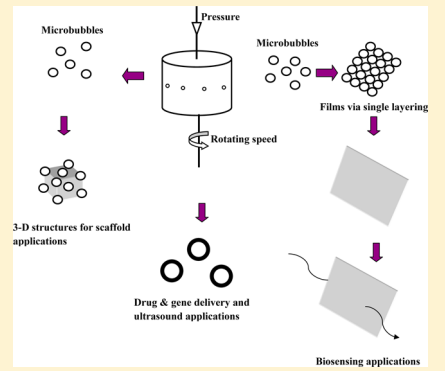
Suntharavathanan Mahalingam,[†] Bahijja Tolulope Raimi-Abraham,[‡] Duncan Q. M. Craig,[‡] and Mohan Edirisinghe*,[†]

[†]Department of Mechanical Engineering, University College London, Torrington Place, London WC1E 7JE, United Kingdom

[‡]School of Pharmacy, University College London, 29–39 Brunswick Square, London WC1N 1AX, United Kingdom

Supporting Information

ABSTRACT: A one-pot single-step novel process has been developed to form microbubbles up to 250 μm in diameter using a pressurized rotating device. The microbubble diameter is shown to be a function of rotational speed and working pressure of the processing system, and a modified Rayleigh–Plesset equation has been derived to explain the bubble-forming mechanism. A parametric plot is constructed to identify a rotating speed and working pressure regime, which allows for continuous bubbling. Bare protein (lysozyme) microbubbles generated in this way exhibit a morphological change, resulting in microcapsules over a period of time. Microbubbles prepared with gold nanoparticles at the bubble surface showed greater stability over a time period and retained the same morphology. The functionalization of microbubbles with gold nanoparticles also rendered optical tunability and has promising applications in imaging, biosensing, and diagnostics.



INTRODUCTION

Microbubbles are an interesting and promising class of materials consisting of a spherical core–shell structure and provide a unique platform for various applications. They have been used in diagnostics, as ultrasound contrast agents because they are gas-filled and smaller than the wavelength of diagnostic ultrasound.^{1,2} These properties transform these small microbubbles into useful entities in focused ultrasound imaging, and site-targeted molecular events *in vivo*, such as inflammation, angiogenesis, and tumor formation, can be assessed.³ Microbubbles have also been used as delivery vehicles in a range of therapeutic applications, including gene therapy, as either simple loaded particles or ultrasound-responsive systems.⁴ Indeed, active pharmaceutical ingredient loaded nanoparticles contained within the shell of the microbubbles combined with ultrasound, magnetic field, light, heat, pH differences, or redox potential differences enable different stimuli–responsive controlled drug delivery at specific sites.^{5–8} In the food industry, surfactant-stabilized microbubbles are used for protein delivery⁹ and recovery.¹⁰ They have been shown to improve the desired properties in food systems, including texture, digestibility, and flavor intensity.^{11,12}

State-of-the-art techniques to prepare microbubbles include conventional methods and newer technological routes.¹³ Sonication and high shear emulsification are well-known conventional methods that can offer high yield and low production cost but possess poor control over the microbubble size and uniformity. The former involves dispersing gas or liquid in a suspension of a suitable coating material using high-intensity ultrasound.¹⁴ The latter requires high shear stirring of

aqueous suspension consisting of immiscible liquid and polymer.¹⁵ Microfluidic devices enable a higher degree of control over the size and polydispersity of microbubbles; however, they operate under limited pressure and flow rate conditions.^{16,17} Coaxial electrohydrodynamic atomization (CEHDA) has been adapted as a well-established bubbling technique, where two flowing fluids are subjected to a high voltage to generate coaxial jetting and, subsequently, break up to form bubbles.¹⁸ Microbubbles prepared using this robust and adaptable technique depend upon fluid properties and processing parameters, such as flow rate and applied voltage. Unlike sonication and microfluidic methods, it gives a high production rate of bubbles and also has the capability to produce near-monodisperse microbubbles.¹⁹ However, this method requires high voltage (kilovolt range), and it might not be suitable for certain healthcare-oriented applications.

Pressurized gyration is a new method comprised of simultaneous centrifugal spinning and solution blowing to form nanofibers in large quantities.²⁰ This technique offers not only manipulation of the polymeric nanofiber size and but also their size distribution by varying the concentration of the polymeric solution, rotating speed, and working pressure. It is a simple but efficient process, allowing for the parallel formation of a multitude of polymer nanofibers with regular morphology.^{20,21} The present work uncovers a new route to form well-characterized protein and nanoparticle-containing protein

Received: June 4, 2014

Revised: July 15, 2014

Published: July 15, 2014

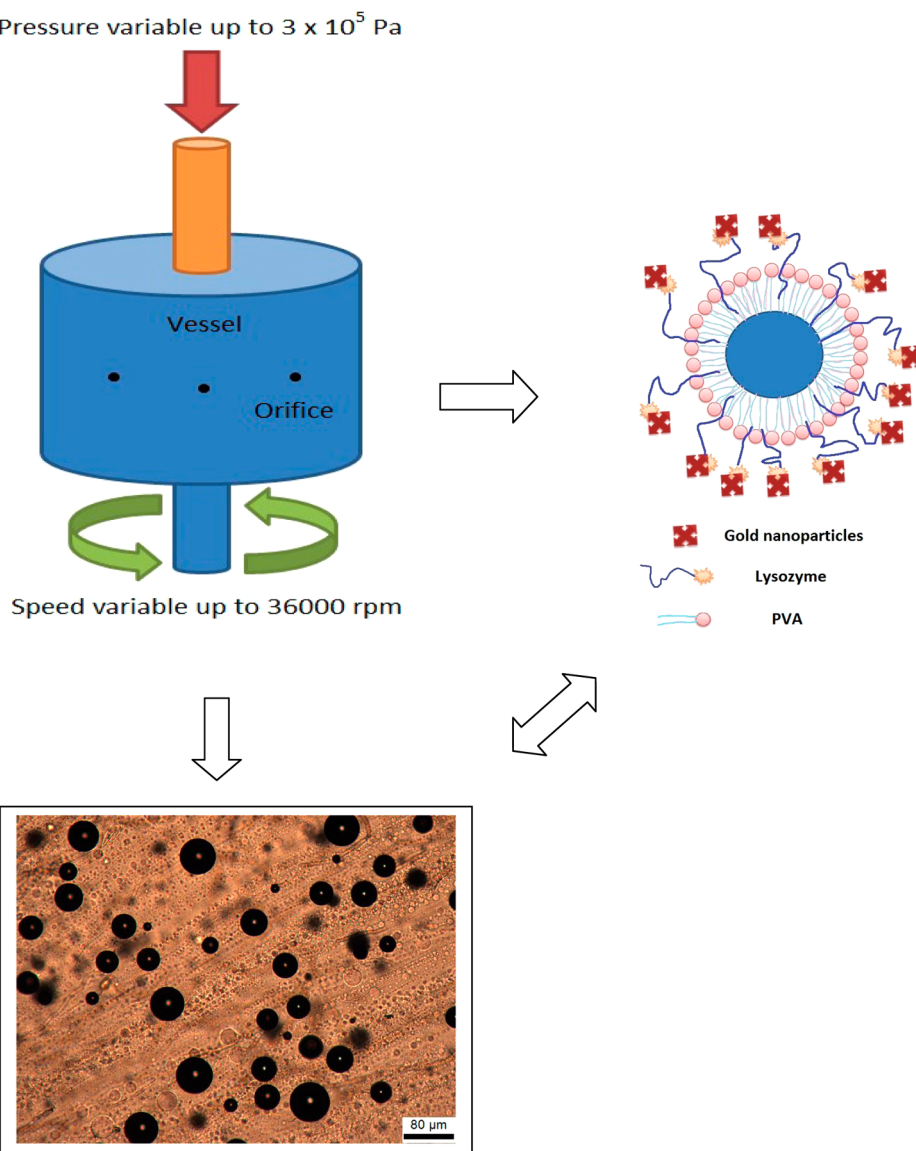


Figure 1. Schematic diagram illustrating the use of pressurized gyration of lysozyme solutions to prepare microbubbles.

microbubbles using pressurized gyration for the very first time. This technique makes use of the destabilizing centrifugal force and the dynamic fluid flow against the stabilizing surface tension of the liquid to form the desired product at very high speed. In this work, we use the well-known polymer poly(vinyl alcohol) (PVA) in combination with a model protein, lysozyme, which is readily assayed for biological activity. We describe the interaction between the two components, which facilitates bubble formation on pressurized gyration.

In the study reported here, a description is also given on how the addition of nanoparticles to the coating layer of the microbubbles affects the stability and the optical tunability of the microbubbles. Gold nanoparticles have excellent chemical stability and biocompatibility with living cells, allowing them to be used as intracellular probes.²² Indeed gold nanoparticles could be used to fabricate quantum dots (Q-dots) that enables the microbubbles to be imaged in a bimodal manner in both fluorescence and ultrasound. Moreover, a careful design of the Q-dot-based microbubbles is a promising delivery vehicle for tracking particles in drug delivery and can provide contrast for photoacoustic imaging, which is a complementary technique to

ultrasound imaging.²³ To this effect, we investigate the sorption of gold nanoparticles onto the bubbles as a means of both influencing physical stability and expanding the range of therapeutic applications of these novel systems.

2. MATERIALS AND METHODS

2.1. Materials. Lysozyme from chicken egg white (molecular weight, $M_w = 14.3$ kDa, ~70 000 units/mg) was obtained from Sigma-Aldrich, U.K., and was used as received. PVA ($M_w = 146\text{--}186$ kDa, 87–89% hydrolyzed) was used as received from Sigma-Aldrich, U.K. Gold nanoparticles (average diameter ~10 nm) in phosphate-buffered saline (PBS) solution were obtained from Sigma-Aldrich, U.K.

2.2. Solution Preparation and Characterization. A 10% (w/v) PVA solution was prepared by dissolving PVA powder in distilled water and mixing using a magnetic stirrer for 2 h at 90 °C. Once 10% (w/v) PVA solution was cooled to ~4 °C, lysozyme powder was dissolved in the PVA solution to produce a 4% (w/v) solution. This solution was subjected to gentle mixing by a magnetic stirrer until lysozyme was completely dissolved. Once samples were prepared, they were stored at 4 °C and used within 24 h. The gold nanoparticle-containing microbubbles were prepared using the gold nanoparticle solution and PVA–lysozyme solution with ratios of 1:10, 1:5, and 2:5

(v/v). The solutions were mechanically stirred at ambient temperature ($\sim 23^\circ\text{C}$) for 2 h prior to pressurized gyration.

The PVA–lysozyme solutions and PVA–lysozyme solutions containing gold nanoparticles were characterized for their surface tension and viscosity after preparation. The static surface tension of the solutions was measured (Wilhelmy plate method) using a Kruss tensiometer K9. Viscosity of the polymer solution was measured using a Brookfield viscometer. All equipment was calibrated before use, and all measurements were performed at ambient temperature.

2.3. Bubble Preparation. Protein and nanoparticle-loaded protein microbubbles were generated using the pressurized gyration process. The experimental setup used at ambient temperature in this study is shown in Figure 1. It consists of a rotary aluminum cylindrical vessel (~60 mm in diameter and ~35 mm in height) containing orifices (~20) on its face. The size of one orifice is 0.5 mm. The vessel and orifice dimensions (including the number of orifices) can be varied to suite. One end of the vessel is connected to a motor, which can generate speeds up to 36 000 rpm. The other end is connected to a gas stream (in our experiments nitrogen was used), the pressure of which can be varied up to 3×10^5 Pa. The high speed of the rotating vessel forms a jet. This jet subsequently breaks up into microbubbles because of the centrifugal force. This breakup mechanism is influenced by the rotating speed of the vessel. To facilitate the collection of microbubbles, a stationary collector made of aluminum foil was placed around the spinning vessel. The gyration process was observed using a high-speed camera (Phantom v7.3, Vision Research). Videos showing the initiation and the subsequent production of the microbubbles in the process are included as Supporting Information.

2.4. Structural Characterization. Microbubble samples were collected using glass microscope slides. These were sealed in a Petri dish and maintained at the ambient temperature. The microbubbles and their physical stability were observed using a Nikon Eclipse ME600 optical microscope over a period of 3 h. More than 100 microbubbles were studied and averaged for each case. ImageJ software [National Institutes of Health (NIH), Bethesda, Maryland, USA version 1.46r] was used for this purpose. The relics of microbubbles formed were also studied using field emission scanning electron microscopy (FE-SEM, model JSM 6301 F). Before imaging, samples were coated with carbon using a sputtering machine (Edwards Sputter S1 50B) for 75 s to minimize charging effects. Ultraviolet-visible spectroscopy studies (UV-vis spectroscopy) were performed on the microbubble samples collected on glass slides. UV-vis absorption spectra were obtained using a PerkinElmer Lambda 35 spectrometer with a 4 nm spectral resolution at 25°C in the 200–700 nm wavelength range.

3. RESULTS AND DISCUSSION

The measured values of surface tension were 67, 65, 62, and 60 mN m^{-1} , and the measured values of viscosity were 3079, 360, 330, and 306 mPa s for PVA–lysozyme and gold nanoparticle containing lysozyme solutions with a ratio of 1:10, 1:5, and 2:5 (v/v), respectively.

The vessel filled with PVA–lysozyme solution rotates about its vertical symmetry axis with a constant rotating speed. Concurrently, nitrogen gas is blown into the vessel. The hybrid external forces create an intense vortex, leading to free surface deformation. Figure 2 shows a schematic illustration of the microbubble formation mechanism by pressurized gyration. When the rotating speed is increased from 10 000 to 36 000 rpm, the air-filled core penetrates deeper and shrinks as it evolves from a stable state (1) to unstable bubbling states (2) and (3). The periodic formation of microbubbles is facilitated by the rotating speed and the fast fluid flow from the vortex tip. The microbubble-forming mechanism is very similar to the co-flow phenomenon observed in electrohydrodynamic bubbling.¹⁹ However, unlike electrohydrodynamic bubbling, microbubbles generated using the pressurized gyration process evolve

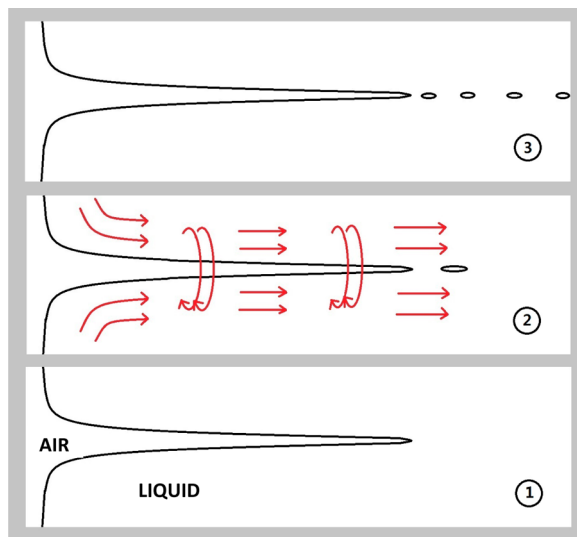


Figure 2. Schematic diagram illustrating the physical mechanism of microbubble formation by pressurized gyration.

from rapid central rotation, which creates a funnel-like down flow near the tip of the vortex, and the centrifugal force, which opposes the final pinch-off.

With the Rayleigh–Plesset equation invoked, the bubble dynamics near the pinch-off region in a collapsing cylindrical cavity could be understood. Assuming that the external fluid is purely radial and has no vorticity, eq 1 can be derived for bubble growth^{24,25}

$$RR'' + \frac{3}{2}R'^2 = \frac{1}{\rho} \left(P_B - \frac{2\sigma}{R} - P_\infty \right) \quad (1)$$

where R is the radius of the bubble, R' and R'' denote dR/dt and d^2R/dt^2 , respectively, t is the time, σ is the surface tension, ρ is the density of the exterior fluid, P_B is the pressure in the bubble, and P_∞ is the pressure at the orifice.

During rotational flow, the velocity components can be denoted by cylindrical polar coordinates v_r , v_θ , and v_z . Assuming that the flow has a rotational symmetry independent of the height, the axial flow can be neglected at the later stage of the collapse ($v_z = 0$), then $v_r = RR'/r$, where r represents the radial distance. When the radial Navier–Stokes equation is integrated with respect to r from R to R_∞ (corresponds to the R value at P_∞), a new eq 2 can be derived

$$\begin{aligned} \frac{d(RR')}{dt} \ln \frac{R}{R_\infty} + \frac{1}{2}R'^2 \left(1 - \frac{R^2}{R_\infty^2} \right) - \frac{2\eta R' + \sigma}{\rho R} \\ = - \int_R^{R_\infty} \frac{V_\theta^2}{r} dr + \frac{P_\infty - P_B}{\rho} \end{aligned} \quad (2)$$

where η denotes the dynamic viscosity.

The reasons behind the collapse of the cylindrical cavity are twofold. The first is the increase of v_θ , which increases the centrifugal pressure and facilitates the collapse. The other is due to volume oscillations of the tip below the neck, and during pinch-off, this volume linearly decreases and creates a constant flux of nitrogen through the neck. This gives rise to very high flow velocities with a Bernoulli pressure reduction $P_\infty - P = \rho_g((v_g/2) + (d\phi/dt))$, where ρ_g is the gas density, v_g is the gas velocity, ϕ is the velocity potential for gas flow, and P is the pressure at a selected distance from the orifice. When the

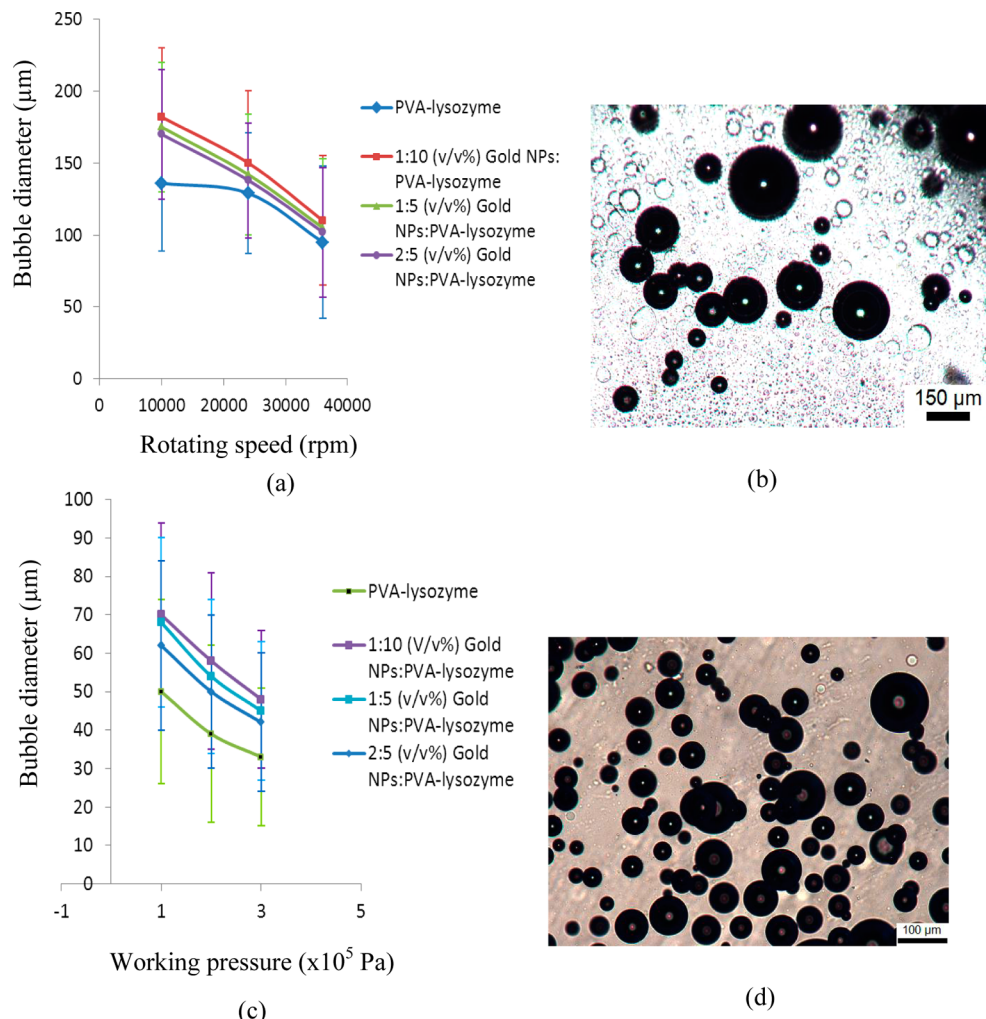


Figure 3. (a) Graph showing the effect of the rotating speed on bubble diameter, at a working pressure of 0.02 MPa. (b) Optical micrograph of microbubbles generated at 10 000 rpm and 0.02 MPa. (c) Graph showing the effect of the working pressure on bubble diameter, at a rotating speed of 36 000 rpm. (d) Optical micrograph of microbubbles processed at 36 000 rpm and 0.1 MPa. NP indicates nanoparticle.

velocity difference between the gas inside the neck and the liquid outside is largest, the pinch-off of bubbles will take place. Indeed, this phenomenon is very similar to that proposed for gas-flow-driven collapse of an asymmetric bubble.²⁶

When the analysis by Burton et al.²⁴ is considered with respect to pinch-off dynamics, the neck radius can be correlated to the viscosity of the liquid during breakup. When the liquid viscosity is >100 mPa s, the bubble neck radius is proportional to the time to break (τ) and decreases smoothly to zero. If the liquid viscosity is <10 mPa s, the radius scales to $\tau^{1/2}$ until an instability develops in the gas bubble, which causes neck rupture and allows for bubbles to tear apart. The lysozyme solutions have viscosities of >100 mPa s; this indicates that the neck diameter will continuously shrink to a minimum until microbubbles are created at the sharp end point of the vortex.

It must be noted that proteins are surface-active molecules and can preferentially adsorb at the water–air interface,²⁷ and this phenomenon can locally modify the surface tension of the system. Thus, eq 1 in our analysis above may need further modification to include this effect on the surface tension.

Figure 3 shows the effect of processing parameters on microbubble size and morphology. Microbubbles up to 250 μm in diameter were produced. A gradual reduction in microbubble diameter was observed by increasing the rotating speed from

10 000 to 36 000 rpm. Thus, for the lysozyme solution, increasing the rotating speed from 10 000 to 36 000 rpm caused the microbubble diameter to reduce from 136 to 95 μm at a working pressure of 0.02 MPa (Figure 3a). Similarly, the microbubble diameter reduced from 182 to 110 μm for 1:10 (v/v%) gold nanoparticle lysozyme solution. The diameter reduction can be tailored by adjusting the nanoparticle content, e.g., from 175 to 105 μm and from 170 to 102 μm for 1:5 and 2:5 (v/v%) gold nanoparticle lysozyme solutions, respectively. The microbubbles produced had a spherical morphology, and the shape of the microbubbles is not compromised even when the rotating speed is increased.

Dramatic reduction in microbubble diameter was observed when increasing the working pressure from 0.1 to 0.3 MPa at a rotating speed of 36 000 rpm (Figure 3c). At a 0.1 MPa working pressure, the average microbubble diameter was 50 μm, and it is nearly halved when the working pressure increased to 0.3 MPa. This is also true for gold–lysozyme microbubbles, where the average microbubble diameter reduced dramatically to 50 μm when increasing pressure at a constant rotating speed. The working pressure has greater impact on microbubble diameter compared to the rotating speed of pressurized gyration. This is also indicated by eq 2, where the rotating

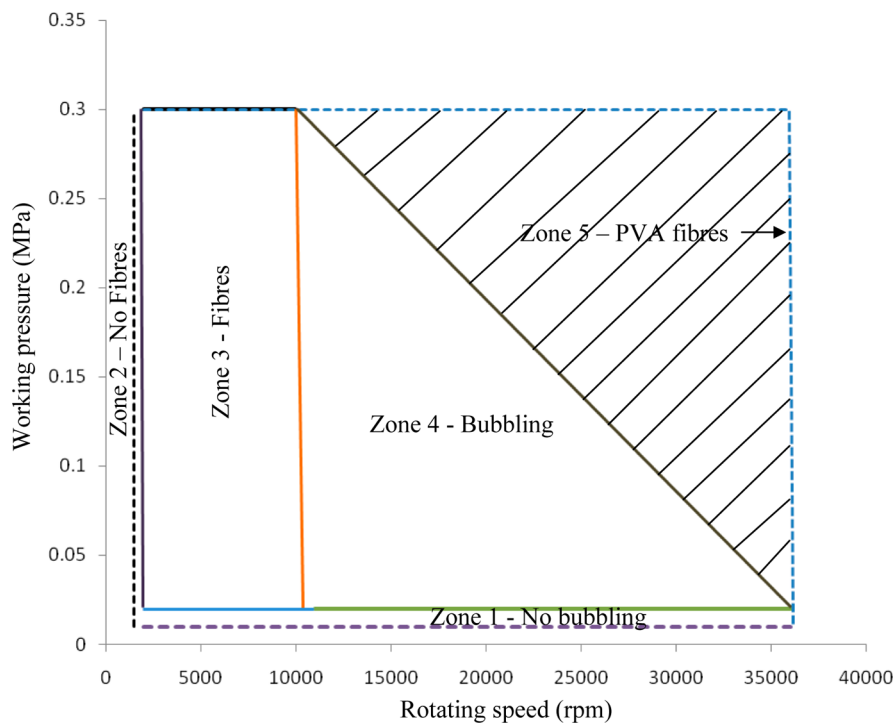


Figure 4. Parametric plot between the rotating speed and the working pressure of PVA–protein solution to show the onset of bubbling (continuous vertical line). Zone 1, no bubbling; zone 2, no fibers; zone 3, fibers; zone 4, bubbling; and zone 5, fiber formable region for PVA solution only.

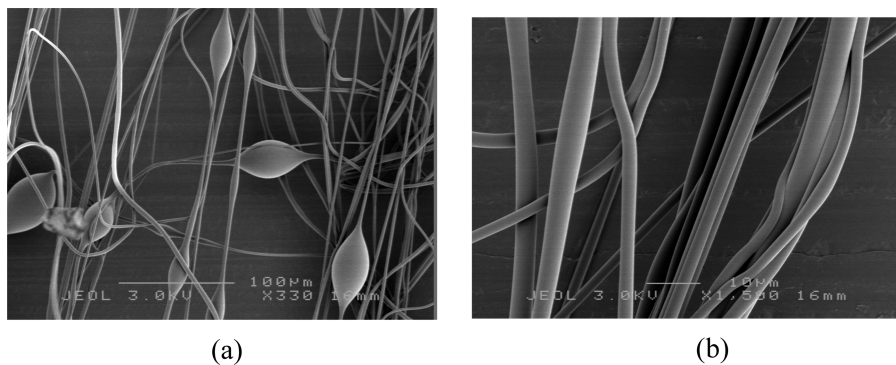


Figure 5. Scanning electron micrographs of fibrous structures obtained at (a) 6000 rpm rotating speed and a 0.2 MPa working pressure and (b) 8000 rpm rotating speed and a 0.2 MPa working pressure.

speed is subdominant on microbubble diameter compared to the working pressure.

From the data presented in Figure 3, it is clear that the microbubbles prepared in this work are coarser ($>8 \mu\text{m}$ diameter) and polydisperse compared to those required for typical biomedical engineering applications, e.g., ultrasound imaging and drug delivery.¹³ For these applications, methods incorporating microfluidics and electrohydrodynamics may be more suited. However, further work is in progress to expand the speed and pressure regimes of pressurized gyration and to introduce flow-controlled gyration. Panels a and c of Figure 3 show that the increase of speed and pressure associated with pressurized gyration can result in the preparation of finer microbubbles. It is also noteworthy that further reduction and size control of the microbubbles can be facilitated by adding surfactants to the liquid carrier^{13,18,19} of the bubbling formulation (PVA in this case), and this strategy will also be exploited in our ongoing work on the preparation of near-monodisperse microbubbles using pressurized gyration.

Figure 4 shows a parametric plot constructed for the PVA–lysozyme solution as a function of the rotating speed and working pressure. The rotating speed varied between 2000 and 36 000 rpm, and the working pressure was changed between 0.01 and 0.3 MPa, to construct this map. This map reveals that there are four distinctive regimes of material discharge in pressurized gyration of PVA–lysozyme solution in the parametric range of the rotating speed and working pressure investigated. Below a certain working pressure (<0.02 MPa), the solution was subjected to normal breakup of liquid jet that produced only droplets, and this is marked as zone 1 in Figure 4. For a working pressure above this critical minimum level and a rotating speed below the critical minimum level (<2000 rpm), there is no bubbling or fiber generation, and this was identified as zone 2. For rotating speeds above this critical minimum level, until the first threshold level is reached, the bubbling mode is not detected; however, when the first threshold rotating speed value is <10 000 rpm and at all working pressures, bead-on-string fibers and straight fiber morphologies were obtained

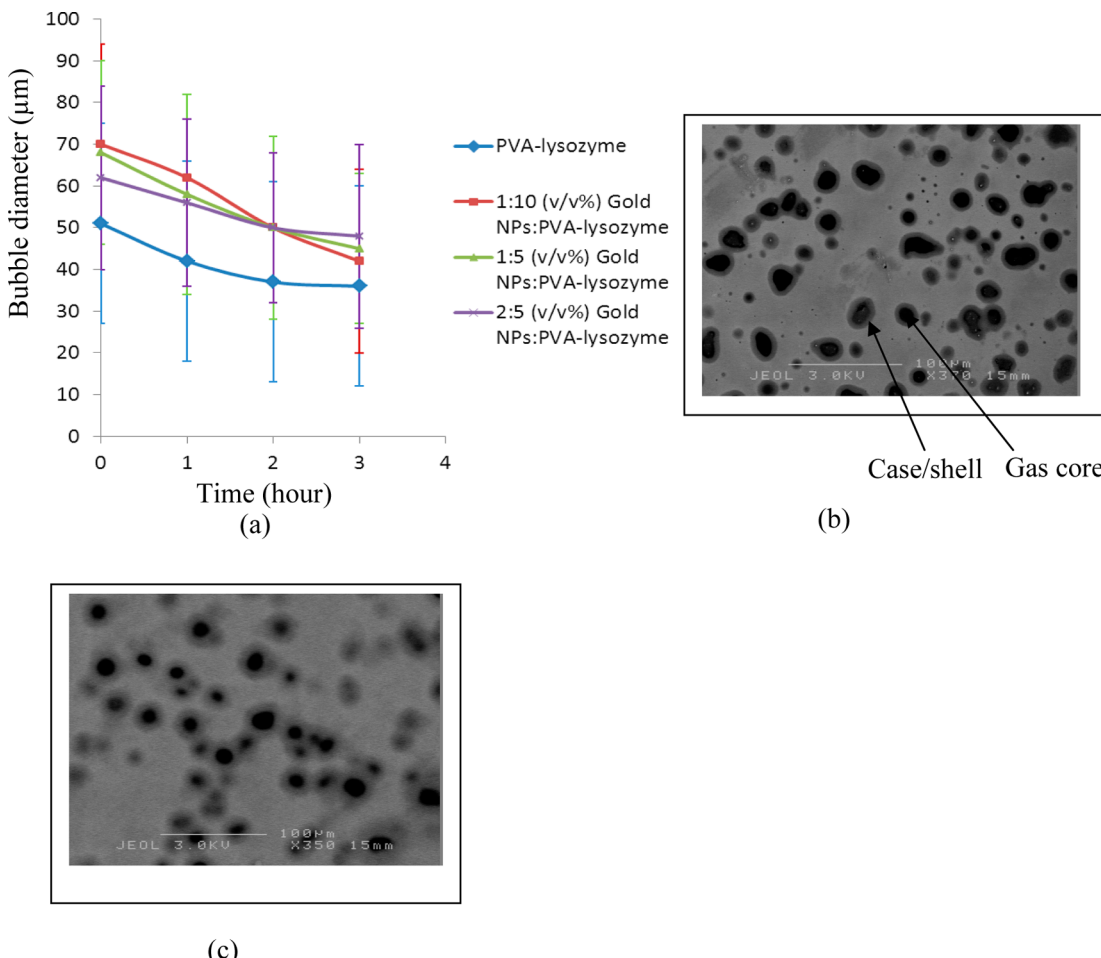


Figure 6. (a) Graph showing the bubble diameter variation with time. (b) Scanning electron micrograph of the lysozyme microbubbles showing the change in morphology of microbubbles and resulting microcapsules after 3 h. (c) Scanning micrograph of the gold nanoparticle–lysozyme microbubbles showing the retention of same morphology after 3 h. At $t = 0$, all microbubbles are spherical (panels b and d of Figure 3). NP indicates nanoparticle.

(panels a and b of Figure 5). This region has been identified as zone 3 in Figure 4. This could be attributed to lower penetration of air in the liquid jet because of the lack of centrifugal force. The central rotation may not have enough force to create a funnel-like down flow near the tip of the vortex and, consequently, lead to bubble pinch-off. Also, under such conditions, the fast liquid flow assists the evaporation of the solvent, enabling immediate solidification to form fibers. Above this first threshold value, until the second threshold value of rotating speed (36 000 rpm), a continuous bubbling regime was found, and this region has been identified as zone 4 in Figure 4. It is noteworthy that PVA furnishes only fibers in a “vast” region enclosed by the dotted lines including zone 5 in Figure 4; therefore, the presence of the protein (lysozyme) is essential to make bubbles. However, to establish whether this is a generic observation, applicable to all proteins, requires further work.

Post-preparation size reduction of various lysozyme microbubbles is shown in Figure 6a. It is clear that the microbubbles prepared from the lysozyme solution reduced in size more than the gold nanoparticle containing lysozyme microbubbles. Among the gold–lysozyme microbubbles, the higher gold concentration showed greater stability. It is well-known that the adsorption of solid nanoparticles on the bubble surface can potentially improve the efficacy of the microbubbles as ultrasound contrast agents by increasing the nonlinear

characteristics of the microbubble acoustic response by a “jamming” effect.²⁸ Thus, surface-active particles with high adsorption energy can generate a sufficiently rigid shell to prevent microbubble shrinkage because of disproportionation. Therefore, the formation of gold nanoparticle containing microbubbles depends upon a delicate balance between the tendency of the partially hydrophobic particles to adsorb at microbubble surfaces and their tendency to aggregate rather than disperse in water.²⁹

The size of the lysozyme microbubbles remained unchanged after 3 h (Figure 6b). However, more detailed examination of the samples showed changes in shape and morphology of the microbubbles. During this period, shrinking and disappearance of the gas core is driven by the Laplace pressure. It is known that the chemical modification and cross-linking of shell materials alters the morphology of the microbubbles.³⁰ Generally, protein shell materials crystallizes and show strong shape anisotropy.³¹ Such shape anisotropy in conjunction with parallel growth directions of multiple crystallites minimizes the overall bending energy and can lead to the distortion of microbubbles.³² In contrast, gold nanoparticle containing lysozyme microbubbles did not exhibit any shape change, suggesting that the lysozyme crystallization is neutralized at the gas–shell interface (Figure 6c).

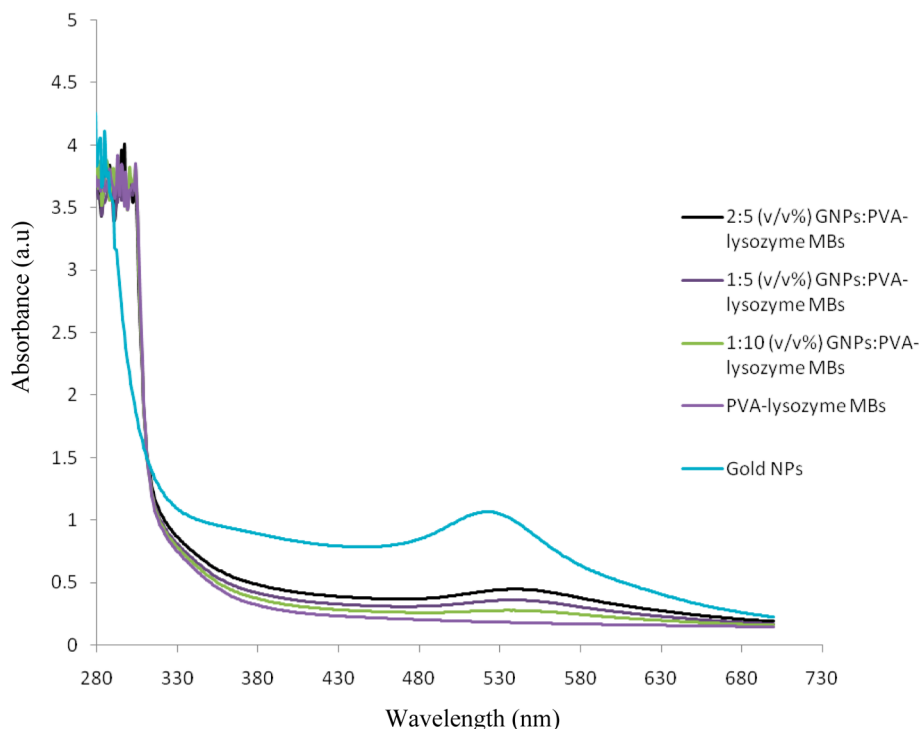


Figure 7. Absorbance spectra (arbitrary units) of a series of nanoparticle containing lysozyme microbubbles. NP, GNP and MB indicate nanoparticle, gold nanoparticle and microbubble, respectively.

Verification of gold nanoparticle binding to the lysozyme microbubbles was provided by UV-vis spectroscopy. Figure 7 shows the absorbance spectra of a series of nanoparticle containing microbubbles. A characteristic surface plasmon resonance band of gold nanoparticles was observed in the spectrum at ~ 530 nm. A red shift and significant broadening in the absorbance spectra for lysozyme microbubbles containing gold nanoparticles was observed and suggests that optical tunability of the microbubbles was achieved and could be exploited in both ultrasound and photoacoustic imaging. There was no clear absorption peak for the PVA-lysozyme microbubbles in the spectrum, providing further evidence of gold nanoparticles on the surface of microbubbles. These dual modality contrast agents are very promising for imaging, biosensing, and diagnostic applications.^{33,34} Our single-step approach to form microbubbles not only offers tunability of the surface energies at the gas-shell interface but also eliminates unnecessary steps to process nanoparticle containing microbubbles, such as in layer-by-layer deposition.³⁵

4. CONCLUSIONS

A novel single-step simple method has been created to produce microbubbles. A modified Rayleigh-Plesset-type equation was derived to explain the bubble-forming mechanism in pressurized gyration. Bubbles up to $250\text{ }\mu\text{m}$ in diameter were produced using a series of protein solutions, and the bubble diameter was a function of the rotating speed and working pressure. Parametric mapping of the process has allowed for the identification of the rotating speed and working pressure needed for continuous bubbling. Stability studies of the microbubbles showed a morphological change in the protein-only microbubbles and enhanced stability in the case of gold nanoparticle containing protein microbubbles. UV-vis spectroscopy results indicate that incorporation of the gold

nanoparticles makes optical tuning of the microbubbles a possibility.

■ ASSOCIATED CONTENT

● Supporting Information

Videos showing the initiation and subsequent production of the microbubbles in the gyration process. This material is available free of charge via the Internet at <http://pubs.acs.org>.

■ AUTHOR INFORMATION

Corresponding Author

*Telephone: +442076793942. E-mail: m.edirisinghe@ucl.ac.uk.

Notes

The authors declare no competing financial interest.

■ ACKNOWLEDGMENTS

The authors thank the Engineering and Physical Sciences Research Council (EPSRC), U.K., for providing the financial support for the exploitation of pressurized gyration research (EP/L023059/1). The authors thank EPSRC for providing the high-speed camera for this work. Adrian Walker (EPSRC) is thanked for help with the high-speed camera use.

■ REFERENCES

- (1) Dayton, P.; Klibanov, A.; Brandenburger, G.; Ferrara, K. Acoustic radiation force in vivo: A mechanism to assist targeting of microbubbles. *Ultrasound Med. Biol.* **1999**, *25*, 1195–1201.
- (2) Stride, E. Physical principles of microbubbles for ultrasound imaging and therapy. *Cerebrovasc. Dis.* **2009**, *27*, 1–13.
- (3) Lindner, J. R. Microbubbles in medical imaging: Current applications and future directions. *Nat. Rev. Drug Discovery* **2004**, *3*, 527–532.
- (4) Cavalli, R.; Bisazza, A.; Lembo, D. Micro- and nanobubbles: A versatile non-viral platform for gene delivery. *Int. J. Pharm.* **2013**, *456*, 437–445.

- (5) Cool, S. K.; Geers, B.; Roels, S.; Stremersch, S.; Vanderperren, K.; Sauders, J. H.; De Smedt, S. C.; Demeester, J.; Sanders, N. N. Coupling of drug containing liposomes to microbubbles improves ultrasound triggered drug delivery in mice. *J. Controlled Release* **2013**, *172*, 885–893.
- (6) Shih, R.; Bardin, D.; Martz, T. D.; Sheeran, P. S.; Dayton, P. A.; Lee, A. P. Flow-focusing regimes for accelerated production of monodisperse drug-loadable microbubbles toward clinical-scale applications. *Lab Chip* **2013**, *13*, 4816–4826.
- (7) Chen, C. C.; Sheeran, P. S.; Wu, S. Y.; Olumolade, O. O.; Dayton, P. A.; Konofagou, E. E. Targeted drug delivery with focused ultrasound-induced blood-brain barrier opening using acoustically-activated nanodroplets. *J. Controlled Release* **2013**, *172*, 795–804.
- (8) Yang, F.; Wang, Q.; Gu, Z.; Fang, K.; Marriott, G.; Gu, N. Silver nanoparticle-embedded microbubble as a dual-mode ultrasound and optical imaging probe. *ACS Appl. Mater. Interfaces* **2013**, *5*, 9217–9223.
- (9) Mahalingam, S.; Meinders, M. B. J.; Edirisinghe, M. J. Formation, stability, and mechanical properties of bovine serum albumin stabilized air bubbles produced using coaxial electrohydrodynamic atomization. *Langmuir* **2014**, *30*, 6694–6703.
- (10) Fuda, E.; Jauregi, P.; Pyle, D. L. Recovery of lactoferrin and lactoperoxidase from sweet whey using colloidal gas aphrons (CGAs) generated from an anionic surfactant, AOT. *Biotechnol. Prog.* **2004**, *20*, 514–525.
- (11) Lau, C. K.; Dickinson, E. Instability and structural change in an aerated system containing egg albumen and invert sugar. *Food Hydrocolloids* **2005**, *19*, 111–121.
- (12) Shen, Y.; Powell, R. L.; Longo, M. L. Interfacial and stability study of microbubbles coated with a monostearin/monopalmitin-rich food emulsifier and PEG40 stearate. *J. Colloid Interface Sci.* **2008**, *321*, 186–194.
- (13) Stride, E.; Edirisinghe, M. Novel microbubble preparation technologies. *Soft Matter* **2008**, *4*, 2350–2359.
- (14) Zhao, Y.; Liang, H.; Mei, X.; Halliwell, M. Preparation, characterisation and in vivo observation of phospholipid-based gas-filled microbubbles containing hirudin. *Ultrasound Med. Biol.* **2005**, *31*, 1237–1243.
- (15) Jiang, B.; Gao, C.; Shen, J. Polylactide hollow spheres fabricated by interfacial polymerization in an oil-in-water emulsion system. *Colloid Polym. Sci.* **2006**, *284*, 513–519.
- (16) Whitesides, G. The origins and the future of microfluidics. *Nature* **2006**, *442*, 368–373.
- (17) Hettiarachchi, K.; Talu, E.; Longo, M. L.; Dayton, P. A.; Lee, A. P. On-chip generation of microbubbles as a practical technology for manufacturing contrast agents for ultrasonic imaging. *Lab Chip* **2007**, *7*, 463–468.
- (18) Farook, U.; Stride, E.; Edirisinghe, M. Preparation of suspensions of phospholipid-coated microbubbles by coaxial electrohydrodynamic atomisation. *J. R. Soc., Interface* **2009**, *6*, 271–277.
- (19) Ekemen, Z.; Chang, H.; Ahmad, Z.; Bayram, C.; Rong, Z.; Denkbas, E. M.; Stride, E.; Vadgama, P.; Edirisinghe, M. Fabrication of biomaterials via controlled protein bubble generation and manipulation. *Biomacromolecules* **2011**, *12*, 4291–4300.
- (20) Mahalingam, S.; Edirisinghe, M. J. Forming of polymer nanofibers by a pressurised gyration process. *Macromol. Rapid Commun.* **2013**, *34*, 1134–1139.
- (21) Raimi-Abraham, B. T.; Mahalingam, S.; Edirisinghe, M. J.; Craig, D. Q. M. Generation of poly(*N*-vinylpyrrolidone) nanofibres using pressurised gyration. *Mater. Sci. Eng., C* **2014**, *39*, 168–176.
- (22) Kennedy, L. C.; Bickford, L. R.; Lewinski, N. A.; Coughlin, A. J.; Hu, Y.; Day, E. S.; West, J. L.; Drezek, R. A. A new era for cancer treatment: Gold–nanoparticle-mediated thermal therapies. *Small* **2011**, *7*, 169–183.
- (23) Shashkov, E. V.; Everts, M.; Galanzha, E. I.; Zharov, V. P. Quantum dots multimodal photoacoustic and photothermal contrast agents. *Nano Lett.* **2008**, *8*, 3953–3958.
- (24) Burton, J. C.; Waldrep, R.; Taborek, P. Scaling and instabilities in bubble pinch-off. *Phys. Rev. Lett.* **2005**, *94*, 184502.
- (25) Oguz, H. N.; Prosperetti, A. Dynamic of bubble-growth and detachment from a needle. *J. Fluid Mech.* **1993**, *257*, 111–145.
- (26) Gordillo, J. M.; Sevilla, A.; Rodriguez-Rodriguez, J.; Martinez-Bazan, C. Axisymmetric bubble pinch-off at high Reynolds numbers. *Phys. Rev. Lett.* **2005**, *95*, 194501.
- (27) Alahverdjieva, V. S.; Grigoriev, D. O.; Fainerman, V. B.; Aksenenko, E. V.; Miller, R.; Möhwald, H. Competitive adsorption from mixed hen egg-white lysozyme/surfactant solutions at the air–water interface studied by tensiometry, ellipsometry, and surface dilatational rheology. *J. Phys. Chem. B* **2008**, *112*, 2136–2143.
- (28) Stride, E.; Pancholi, K.; Edirisinghe, M. J.; Samarasinghe, S. Increasing the nonlinear character of microbubble oscillations at low acoustic pressures. *J. R. Soc., Interface* **2008**, *5*, 807–811.
- (29) Du, Z.; Bilbao-Montoya, M. P.; Binks, B. P.; Dickinson, E.; Ettelaie, R.; Murray, B. S. Outstanding stability of particle-stabilized bubbles. *Langmuir* **2003**, *19*, 3106–3108.
- (30) Cavalieri, F.; Zhou, M.; Caruso, F.; Ashokkumar, M. One-pot ultrasonic synthesis of multifunctional microbubbles and microcapsules using synthetic thiolated macromolecules. *Chem. Commun.* **2011**, *47*, 4096–4098.
- (31) Ratanabanangkoon, P.; Gropper, M.; Merkel, R.; Sackmann, E.; Gast, A. P. Two-dimensional streptavidin crystals on giant lipid bilayer vesicles. *Langmuir* **2002**, *18*, 4270–4276.
- (32) Ratanabanangkoon, P.; Gropper, M.; Merkel, R.; Sackmann, E.; Gast, A. P. Mechanics of streptavidin-coated giant lipid bilayer vesicles: A micropipette study. *Langmuir* **2003**, *19*, 1054–1062.
- (33) Dove, J. D.; Murray, T. W.; Borden, M. A. Enhanced photoacoustic response with plasmonic nanoparticle-templated microbubbles. *Soft Matter* **2013**, *9*, 7743–7750.
- (34) Cavalieri, F.; Micheli, L.; Kaliappan, S.; Teo, B. M.; Zhou, M.; Palleschi, G.; Ashokkumar, M. Antimicrobial and biosensing ultrasound-responsive lysozyme-shelled microbubbles. *ACS Appl. Mater. Interface* **2013**, *5*, 464–471.
- (35) Cavalieri, F.; Ashokkumar, M.; Grieser, F.; Caruso, F. Ultrasonic synthesis of stable, functional lysozyme microbubbles. *Langmuir* **2011**, *24*, 10078–10083.